Therapeutics, Targets, and Chemical Biology

Cancer Research

Focused Ultrasound Delivers Targeted Immune Cells to Metastatic Brain Tumors

Ryan Alkins[1,3], Alison Burgess[1], Milan Ganguly[1], Giulio Francia[2], Robert Kerbel[2,3], Winfried S. Wels[4], and Kullervo Hynynen[1,3]

Abstract

Natural killer (NK) cells are cytotoxic lymphocytes involved in innate immunity. NK-92, a human NK cell line, may be targeted to tumor-associated antigens in solid malignancies where it exhibits antitumor efficacy, but its clinical utility for treating brain tumors is limited by an inability to cross the blood–brain barrier (BBB). We investigated the potential for focused ultrasound (FUS) to deliver targeted NK-92 cells to the brain using a model of metastatic breast cancer. HER2-expressing human breast tumor cells were implanted into the brain of nude rats. The NK-92-scFv(FRP5)-zeta cell line expressing a chimeric HER2 antigen receptor was transfected with superparamagnetic iron oxide nanoparticles before intravenous injection, before and following BBB disruption using focused ultrasound (551.5 kHz focused transducer, 0.33 MPa average peak rarefaction pressure) in the presence of a microbubble contrast agent. Baseline and posttreatment 1.5T and 7T MR imaging was done, and histology used to identify NK-92 cells post-mortem. Contrast-enhanced MRI showed reproducible and consistent BBB disruption. 7T MR images obtained at 16 hours posttreatment revealed a significant reduction in signal indicating the presence of iron-loaded NK-92 cells at the tumor site. The average ratio of NK-92 to tumor cells was 1:100 when NK cells were present in the vasculature at the time of sonication, versus 2:1,000 and 1:1,000 when delivered after sonication and without BBB disruption, respectively. Our results offer a preclinical proof-of-concept that FUS can improve the targeting of immune cell therapy of brain metastases. *Cancer Res; 73(6); 1892–9.* ©*2012 AACR.*

Introduction

As many as 30% of breast cancer patients develop central nervous system (CNS) metastasis (1), for which current breast cancer therapies are inadequate (2). Systemic therapies are hindered by the cerebral capillary endothelium, which is interconnected by tight junctions, forming the blood–brain barrier (BBB; ref. 3). The BBB normally allows passage of only small lipophilic compounds into the CNS. Within the tumor there is a variably more permeable blood–tumor barrier (BTB), but this still significantly hinders treatment (4). Furthermore, P-glycoprotein, expressed by cerebral capillaries and tumor cells, results in the efflux of many chemotherapeutic agents that would otherwise have therapeutic activity (5). As a result, intravenously delivered agents currently have limited efficacy in the treatment of brain metastasis (2).

Breast cancers with HER2 amplification are more aggressive, have a higher risk of CNS metastasis, and poorer prognosis (5, 6). The HER2 receptor is thought to be involved in signaling pathways regulating cell growth and differentiation (6). Antibodies targeted to HER2 have resulted in improved tumor control and survival in HER2-amplified breast cancers (7), whereas the HER2 inhibitor lapatinib has shown improved progression-free survival in advanced HER2-positive breast cancers (8). Similar targeted treatments have been investigated in preclinical models using natural killer (NK) cells, the cytotoxic lymphocytes involved in the innate immune response to malignant cells (9). The HER2-specific NK-92-scFv(FRP5)-zeta cell line is a human NK-92 cell line modified to express a chimeric HER2 antigen receptor (10). It has been shown to localize to extracranial HER2-amplified breast cancers in animal models and cause selective tumor cell death (10, 11, 12). However, neither HER2-targeted antibodies (13, 14) nor NK-92 cells are able to cross the BBB to a significant extent, whereas lapatinib is susceptible to P-glycoprotein and breast cancer resistance protein (15).

We investigated the feasibility of delivering HER2-specific NK-92 cells to the brain with focused ultrasound (FUS) because in contrast to antibodies and inhibitors, these cells are targeted, possess direct cytolytic activity, and are unaffected by efflux channels (9). Using ultrasound bursts at sub-megahertz frequencies through the intact skull, in combination with timed intravenous (i.v.) injections of encapsulated perfluorocarbon microbubbles, the permeability of the cerebral vasculature can be noninvasively increased in targeted, focal regions (16, 17). Cavitation of microbubbles under the influence of ultrasound seems to cause temporary mechanical disruption

Authors' Affiliations: [1]Physical Sciences Platform, [2]Biological Sciences Platform, Sunnybrook Research Institute; [3]Medical Biophysics, University of Toronto, Toronto, Ontario, Canada; and [4]Chemotherapeutisches Forschungsinstitut Georg-Speyer-Haus, Frankfurt, Germany

Corresponding Author: Ryan Alkins, Sunnybrook Research Institute, 2075 Bayview Ave, C713, Toronto, Ontario, Canada M4N 3M5. Phone: 416-480-6100 ext 89420; Fax: 416-480-4696; E-mail: ralkins@sri.utoronto.ca

doi: 10.1158/0008-5472.CAN-12-2609

of endothelial tight junctions, and increased para- and transcellular passage of molecules from the blood into the brain (18, 19). Contrast-enhanced magnetic resonance imaging (MRI) can be used to identify the regions of contrast extravasation and confirm BBB and BTB disruption (BBBD; ref. 17). This technique has been shown to increase the penetration of a number of therapeutic agents into the brain in rodent models (20, 21, 22) and has recently been shown to be safe in nonhuman primates (23).

We examined whether HER2-specific NK-92-scFv(FRP5)-zeta cells injected intravenously could be delivered to the brain using MRI-guided FUS in a xenograft HER2-expressing breast metastasis model. By transfecting the HER2-specific NK-92 cells with superparamagnetic iron oxide (SPIO) nanoparticles, we were able to track their accumulation at the tumor site. Furthermore, we quantified the density of effector-to-tumor cells to confirm that the number was sufficient to successfully treat a tumor, and assessed the cytolytic function of HER2-specific NK-92 cells following exposure to ultrasound *in vivo*.

Materials and Methods

Cell lines and culture

Human HER2-expressing MDA-MB-231 breast tumor cells were cells isolated from brain metastases, secondary to a primary tumor implanted in a mouse mammary fat pad, and transfected to express HER2 as previously reported (24). MDA-MB-231-HER2 cells were maintained in RPMI 1640 media supplemented with 10% FBS (Wisent). For implantation, cells were collected, centrifuged, and resuspended in Hanks' balanced salt solution (Wisent) at a concentration of 10^3 cells/μL. HER2 expression was confirmed using immunocytochemistry. MDA-MB-231-HER2 cells were plated on 8-well chamber slides (Nunc) for 24 hours and then fixed with 4% paraformaldehyde for 10 minutes at room temperature. Cells were treated with blocking solution containing 1% donkey serum for 1 hour followed by incubation with primary rabbit anti-HER2 (Thermo Fisher Scientific) overnight. Slides were washed and incubated with donkey antimouse Cy3 for 1 hour, and coverslipped. Fluorescent images were captured with a Zeiss Axiovert microscope.

The human cell line, NK-92 (American Type Culture Collection), was virally transduced to stably express a chimeric antigen receptor specific to HER2 (10). The antigen receptor expression was confirmed by fluorescence-activated cell sorter (FACS) analysis (10). HER2-specific NK-92-scFv(FRP5)-zeta cells were maintained in X-VIVO 10 medium (Lonza) supplemented with 5% heat- inactivated human serum (Cedarlane), 0.6 mg/mL G418 (Wisent) and 100 μg/mL IL-2 (R&D systems). Expression of CD45 was evaluated on a cell smear of targeted cells using mouse antihuman CD45 (R&D systems) and the procedures described earlier. Before use *in vivo*, HER2-specific NK-92 zeta cells were labeled with SPIO nanoparticles (diameter 10–50 nm) as MRI contrast. A total of 100 μg Fe_3O_4 (Sigma-Aldrich) was combined with Lipofectamine transfection reagent (Invitrogen) for 30 minutes and subsequently added to 10^6 NK-92 cells in normal media for 24 hours at 37°C (11). Cells were collected, centrifuged, and resuspended in sterile, physiological saline at a concentration of 10^7 cells/mL for injection *in vivo*. Transfection efficiency was estimated using light microscopy to identify SPIO nanoparticles within the cell cytoplasm.

Tumor implantation

All procedures were approved by the Sunnybrook Research Institute Animal Care and Use Committee and conformed to the guidelines set out by the Canadian Council on Animal Care. General anesthesia was induced and maintained with isofluorane in 250 to 300 g male athymic nude rats (Charles River). A burrhole was fashioned in the skull and cells were implanted in the left frontal striatum with a Hamiton syringe guided by stereotactic frame, at a depth of 4 mm from the cortical surface. MDA-MB-231-HER2 cells were combined with a 1% agar solution at 37°C to a final density of 10^3 cells/μL, and 10 μL were injected (25). Animals underwent serial MRI imaging and the tumors treated once they had reached 1.5 to 2 mm in size.

MRI-guided focused ultrasound

In preparation for BBBD, animals were anesthetized with ketamine (90 mg/kg) and xylazine (10 mg/kg). A 22-gauge cannula was inserted into the tail vein and the head of the animal shaved and chemically depilated. Definity ultrasound contrast (Lantheus Medical Imaging) was prepared as directed by the manufacturer by warming to room temperature and activating in the proprietary agitator (VIALMIX; Lantheus Medical Imaging). It was then diluted 1:10 in 0.9% saline. Animals were positioned supine on the in-house designed 3-axis positioning system (26) and fixed in place with a bite bar and lower extremity restraints. The head was coupled to a 551.5 kHz single element focused ultrasound transducer ($F = 0.8$, $R = 10$ cm) through a bath of degassed water and surrounded by an in-house manufactured 3 × 5 cm (inner dimensions) rectangular RF surface coil (Fig. 1). The focal spot size for this transducer, characterized by the full width at half maximum of the beam pressure profile, corresponded to a diameter of 3.0 mm in the axial plane (x–y plane in Fig. 1) by 12.5 mm in the beam direction (z-direction in Fig. 1). The tumors were therefore completely encompassed by the focus.

Targeting and registration images were acquired with a 1.5T clinical MRI scanner (Signa; GE Healthcare). All animals underwent baseline T2- (FOV 6 cm, 128 × 128 matrix, slice thickness 1 mm, NEX 2, ETL 4, TR 2000 milliseconds, TE 75 milliseconds) and T1-weighted (FOV 6 cm, 128 × 128 matrix, slice thickness 1 mm, NEX 6, ETL 4, TR 500, TE ∼10 milliseconds) MR imaging, including a contrast enhanced (0.2 mL/kg; Omniscan, GE Healthcare) sequence, to identify the tumor. Following MRI and ultrasound coregistration, the computer-controlled 3-axis positioning system allowed the focal spot of the transducer to be positioned at any location within the brain. BBBD was done (10 milliseconds pulses, 1 Hz pulse repetition frequency, 120 seconds total duration) using a controller to modulate the acoustic power (0.33 MPa average estimated peak rarefaction pressure in the brain; range 0.32–0.35 MPa; ref. 27). The estimated *in situ* pressure was determined assuming 73% transmission through the rat skull (28) and

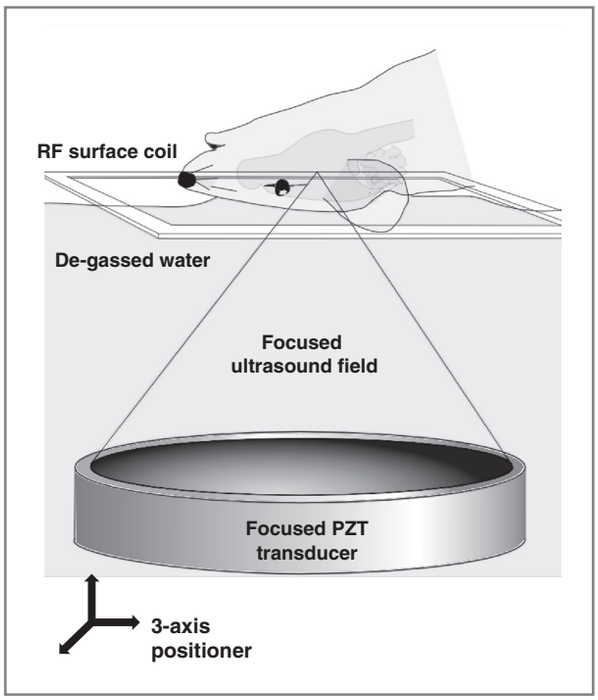

Figure 1. The experimental MRI-guided FUS setup. The anesthetized animal was positioned supine over an MRI RF surface coil and coupled to the piezo-ceramic focused transducer through a bath of de-gassed water. The transducer was repositioned with the aid of a computer-controlled 3-axis positioning system, allowing the ultrasound focus to reach any point within the brain. The entire setup fits in the bore of the 1.5T MR scanner, allowing for coordinate coregistration, targeting, and confirmation of BBBD.

an attenuation coefficient of 5.0 Np/m/MHz in brain (16) with an acoustic path length of 5 mm.

A 60 seconds infusion of diluted Definity (0.2 mL/kg) was administered via the tail vein catheter simultaneously with the onset of the sonication. Posttreatment T2- and contrast-enhanced T1-weighted sequences were acquired to assess the location and degree of BBBD. To detect iron oxide–labeled cells, imaging was conducted on a 7T MRI (BioSpec 70/30 USR; Bruker BioSpin) fitted with gradient and shim insert (BGA-S; Bruker BioSpin) and using a circularly polarized rat brain RF coil (Bruker BioSpin). Both T2-weighted (TR = 3,000 milliseconds, TE = 37.2 milliseconds, flip angle = 180°) and T2*-weighted (8 echo train, TR = 1,000 milliseconds, TE = 24 milliseconds, flip angle = 30°) sequence were conducted. The change in signal intensity within the tumor on T2*-weighted images (19 milliseconds echo) after the treatment with SPIO-labeled cells, compared with pretreatment, was quantified.

Treatment groups

Three treatment arms received intravenous injection of 10^9 targeted NK-92 cells/m^2 body surface area (estimated from body weight), on the order of the number of cells delivered in previous phase I/II trials (29, 30). Group 1 ($n = 4$) received HER2-specific NK-92 cells but no BBBD. Group 2 ($n = 4$) received HER2-specific NK-92 cells following BBBD. Group 3 ($n = 5$) had HER2-specific NK-92 cells injected immediately before BBBD. The experimental timeline for the 3 treatment groups is shown in Fig. 2.

Histologic analysis

Animals were sacrificed by euthanyl injection 12 to 16 hours after treatment. Brains were removed, fixed in 10% neutral buffered formalin, and serial 4 μm coronal sections cut at 250 μm levels. All sections were stained with hematoxylin and eosin (H&E) for morphologic analysis, and Prussian blue for the detection of SPIO nanoparticles (Polysciences Inc.). Immunohistochemistry (IHC) using the polymerized reporter enzyme staining system (Vector Laboratories) was used to detect CD45 (mouse antihuman, 1:200; R&D Systems), perforin (mouse antihuman, 1:10; Abcam),

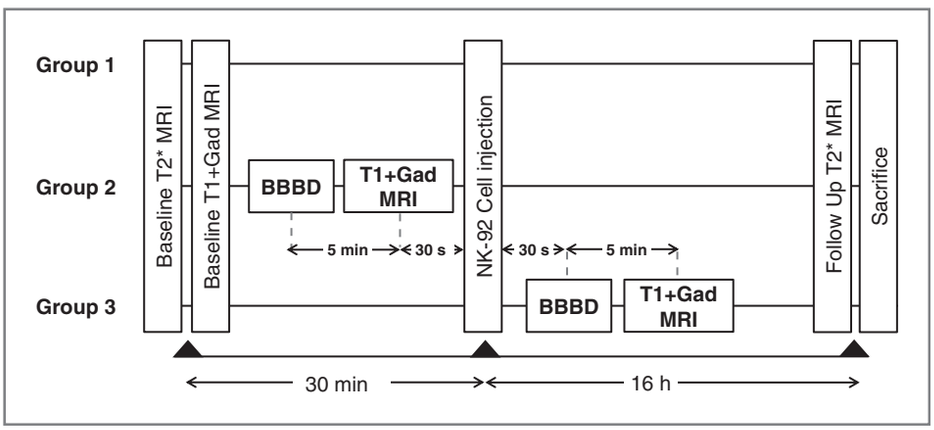

Figure 2. Experimental timeline for the three groups. All groups initially underwent baseline imaging to assess the tumor size and location. In group 1 (control), this was followed by injection of SPIO nanoparticle–labeled HER2-specific NK-92 cells. Follow-up imaging was done at 16 hours following cell injection and immediately before sacrifice. Group 2 underwent BBBD, followed 5 minutes later by T1-weighted MRI with contrast to assess the change in contrast extravasation. Cells were then injected approximately 30 seconds after the completion of the imaging. In group 3, cells were injected via the tail vein and BBBD initiated 30 seconds after the injection. T1-weighted MRI was done 5 minutes post-BBBD again to assess the change in contrast extravasation. Both groups 2 and 3 were imaged at 16 hours after the cell injection and immediately euthanized.

and granzyme B (rabbit antihuman, 1:100; Abcam). Sections were digitized with a Mirax Scanner (Zeiss) and analyzed using Pannoramic Viewer (v.1.15; 3DHISTECH). For each animal, 4 sequential levels were analyzed by 2 blinded investigators. HER2-specific NK-92 cells were identified by CD45 expression and intracellular iron on Prussian blue histochemistry done on serial sections at each level. Effector cells within the tumor boundary were counted and expressed as a percentage of the number of tumor cells in each section. Effector cells outside of the tumor region were ignored for this analysis. The average ratio (effector per 100 tumor cells, mean ± SEM) was then calculated for each treatment group.

Cytotoxicity assay

Cytotoxicity assays were conducted to determine the extent of MDA-MB-231-HER2 cell death achieved using differing effector-to-tumor cell ratios. 10^6 MDA-MB-231-HER2 cells were plated and maintained for 2 hours at 37°C. Serial dilutions (10^6, 10^5, 10^4) of HER2-specific NK-92 cells were prepared in fresh medium and added to the MDA-MB-231-HER2 cell layer (corresponding to effector-to-tumor cell ratios of 1:1, 1:10, and 1:100). At 2 and 24 hours, the cells were rinsed, collected, and analyzed using Trypan blue cell exclusion dye. Results were expressed as the ratio of dead cells to the total number of cells counted. Similar experiments were completed after iron transfection.

Statistical analysis

GraphPad Prism 5 (GraphPad Software) was used for statistical analysis. Student *t* test was used to compare the mean ± SEM of 2 groups and the mean ± SEM of 3 or more groups were compared with 1-way ANOVA and Tukey post-test. Statistical significance was noted if $P < 0.05$.

Results

Before implantation, HER2 expression in MDA-MB-231-HER2 cells was determined to be 80% using IHC. CD45 expression by HER2-specific NK-92 cells was found to be 100% using IHC. The average transfection efficiency of HER2-specific NK-92 cells with SPIO nanoparticle was 80% and did not affect their cytolytic function.

Representative pre- and posttreatment contrast-enhanced T1-weighted MR images are shown in Fig. 3A and B. The degree of contrast enhancement following BBBD was relatively uniform and was double that of the tumor region before treatment (34 ± 10% vs. 17 ± 8%, $P = 0.01$). All animals tolerated the cell injection and BBBD without complication, and recovered from general anesthesia to their pretreatment condition. No abnormal behavior was noted in the 16-hour interval between treatment and sacrifice.

Posttreatment 7T MR imaging detected HER2-specific NK-92 cells at the tumor site in group 3 by a −17 ± 4% change in the signal intensity versus a 14 ± 7% change in group 1 ($P < 0.001$). Representative pre- and posttreatment T2*-weighted sequences are shown in Fig. 3A and B. The differences between other groups were not found to be statistically significant ($P > 0.05$; Fig. 4C).

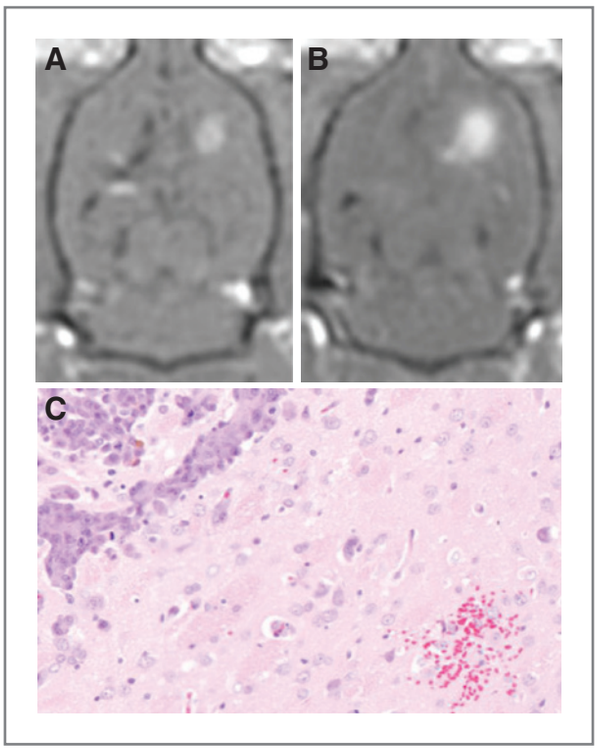

Figure 3. The results of blood–brain barrier disruption with FUS. A, B, representative T1-weighted MR images with Omniscan contrast of the tumor before and after BBBD. The average enhancement of untreated tumors was 17 ± 8% but increased to 34 ± 10% following exposure to ultrasound and microbubbles (mean ± SD, $P < 0.05$). C, a small region of erythrocyte extravasation was seen in one of the treatment animals. There was no further evidence of tissue injury.

After animal sacrifice, H&E stained sections were examined for tissue injury. One FUS-treated animal had a small region of erythrocyte extravasation adjacent the tumor (Fig. 3C). HER2-specific NK-92 cells were counted using both CD45 expression and the presence of intracellular iron on Prussian blue stained sections, and expressed as number of effector cells per 100 tumor cells. Without BBBD, a very small number of HER2-specific NK-92 cells localized to the tumor (group 1, 0.09 ± 0.11; Fig. 5), and almost equally few reached the tumor when BBBD was done before the injection of cells into the circulation (group 2, 0.21 ± 0.15; Fig. 5). In contrast, the ratio of HER2-specific NK-92-to-tumor cells was increased 5-fold when the former were circulating at the time of sonication compared with injection afterward (group 3, 0.95 ± 0.23; Fig. 5). The number of effector cells accumulating in the sonicated tumors in group 3 corresponds to approximately 0.34% of the total number of cells injected. This increase was statistically significant when compared with the former 2 groups ($P < 0.01$; Fig. 5B). There was no statistical difference between groups 1 and 2. More dense accumulations of cells were observed around arterioles and venules in group 3, with an effector-to-tumor ratio significantly greater than the volume-averaged value (Fig. 6A and C). Furthermore, cells were identified outside of the tumor boundary in a number of sections in group 3 but not

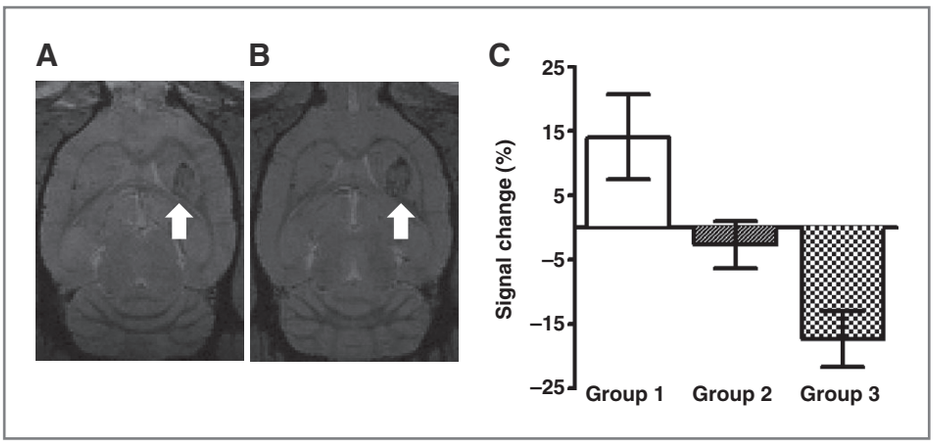

Figure 4. HER2-specific NK-92 cell detection with 7T MRI. A, a baseline axial T2*-weighted MR image from group 3 is shown with the tumor identified in the left frontal striatum (white arrow). B, the corresponding posttreatment image shows a signal reduction at the tumor site (white arrow). C, the average signal intensity change (mean ± SEM) at the tumor site after treatment. A negative change suggests the accumulation of iron-labeled effector cells. There was a statistically significant difference between groups 3 and 1.

counted in the analysis; theoretically these cells could migrate to the tumor and contribute to a higher effector to tumor cell ratio.

We also examined whether HER2-specific NK-92 cells circulating before BBBD would be negatively affected by interactions with oscillating microbubbles at the ultrasound focus. Perforin and granzyme B IHC showed that HER2-specific NK-92 cells retained their function after translocation into the brain. Figure 7A illustrates a targeted NK-92 cell within the tumor having released granzyme B, which can be identified within the cytoplasm of surrounding tumor cells. Perforin was similarly seen in the extracellular space surrounding effector cells and within the cytoplasm of tumor cells. Tumor cells undergoing apoptosis after interaction with HER2-specific NK-92 cells are seen in Fig. 7A and B.

Cytotoxicity assays were conducted to estimate whether a sufficient number of HER2-specific NK-92 cells accumulated at the tumor sites following BBBD for efficient tumor cell lysis. At the 2-hour time point there was a higher proportion of dead MDA-MB-231-HER2 cells in the 1:10 and 1:1 NK-92: tumor groups, but at 24 hours there were no statistically significant differences between the 3 different starting ratios ($P > 0.05$; Fig. 7C).

Discussion

HER2-specific immune cells have showed *in vivo* efficacy against HER2-amplified extracranial tumors when injected into the blood stream (10–12). Intracranially, however, successful treatment has necessitated direct injection of targeted immune cells into the tumor through a burrhole in the skull (31, 32). In this study, we have showed for the first time the feasibility of using MRI-guided FUS to allow intravenously injected HER2-specific NK-92 cells access to tumors in the brain. SPIO-laden effector cells were detected at the tumor site with T2*-weighted MRI in group 3. Although an average signal decrease over the tumor volume was detected, heme

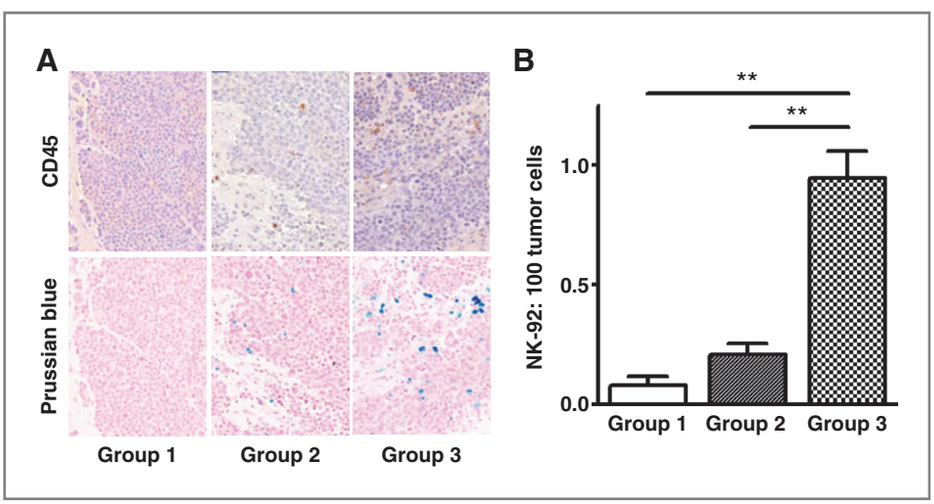

Figure 5. Histologic quantification of HER2-specific NK-92 cells accumulating at the tumor site. A, effector cells were colocalized with CD45 IHC (top) and Prussian blue histochemistry (bottom) in the three experimental groups. B, HER2-specific NK-92 cells reaching the tumor were quantitatively assessed (mean ± SEM). When NK-92 cells were injected before BBBD, the number reaching the tumor was significantly higher than if they were injected after or without BBBD (group 3 vs. groups 1 and 2: 0.95 ± 0.23 vs. 0.09 ± 0.11, 0.21 ± 0.15, $P < 0.01$). There was no statistical difference between groups 1 and 2. These results are in agreement with the iron-sensitive MR imaging in Fig. 4.

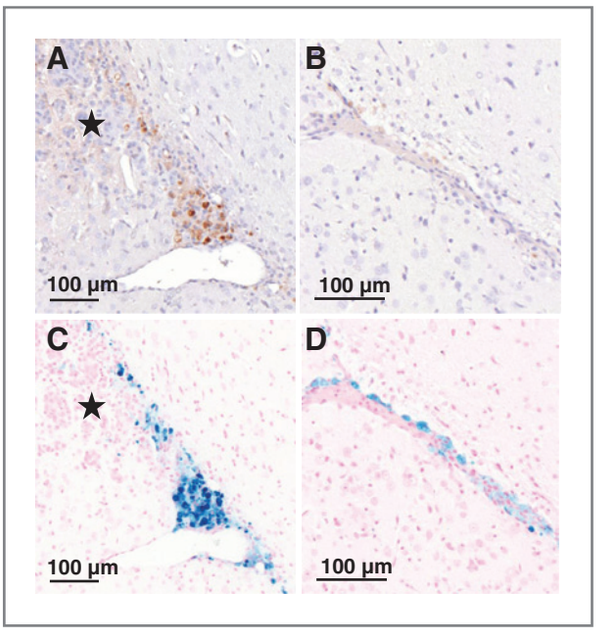

Figure 6. FUS causes the translocation of HER2-specific NK-92 cells from the vasculature into the brain and tumor when they are present in the circulation at the time of BBBD. A, CD45 IHC depicting a vessel from which a large number of cells have extravasated and seem to track to the tumor (star). B, the corresponding Prussian blue stained section is shown, colocalizing the HER2-specific NK-92 cells. C, a normal capillary adjacent the tumor but within the sonicated region shows HER2-specific NK-92 cells forced to the adluminal surface of the vessel. FUS results in HER2-specific NK-92 cells circumventing both the BBB and BTB. D, the corresponding Prussian blue section. These cell distributions were seen exclusively in group 3 animals.

breakdown products from the stereotactic implantation of tumor cells may have complicated the analysis. The presence of intratumoral heme products in human patients could similarly interfere with the *in vivo* tracking of SPIO nanoparticle-labeled effector cells.

The order of BBBD and cell injection was found to have a significant impact on the number of HER-specific NK-92 cells reaching the tumor (Fig. 5A and B). The exact mechanisms underlying this increase in HER2-targeted NK-92 cell accumulation in the sonicated tumor volume are unknown. Despite identical ultrasound exposures, the presence of HER2-targeted NK-92 cells in the circulation at the time of BBBD resulted in an almost 5-fold increase in the ratio of effector-to-tumor cells. One possibility is that inter-endothelial clefts may be larger during the sonication, facilitating the extravasation of effector cells present during BBBD. It is uncertain whether the effect of BBBD on endothelium stimulates or inhibits diapedesis, but if priming of the endothelium was the sole mechanism responsible for effector cell extravasation at the tumor site, the order of cell injection should have made little difference. It has been previously reported that FUS stimulates the release of nitric oxide (NO) from endothelial cells *in vitro* (33, 34), as well as increases the expression of caveolin-1 *in vivo* (35), and thus it is conceivable that BBBD could affect the expression of proteins involved in leukocyte adhesion. Furthermore, the interaction of ultrasound and microbubbles with the HER2-targeted NK-92 cells may play a role. Microbubbles undergoing stable cavitation are known to generate shear stresses (36–38), and increased fluid shear stresses have a number of *in vitro* effects on activated leukocytes including increased adhesion (39, 40), deformability (41), motility (42), and transmigration (42, 43). Although speculatory, it is possible that circulating HER2-specific NK-92 cells are more likely to adhere to endothelium and extravasate after exposure to fluid shear stresses generated by microbubbles at the ultrasound focus. These *in vitro* studies typically required fluid shear stresses in the setting of an activated endothelium, and therefore from the group 2 results (where the endothelium was exposed to FUS but the HER2-specific NK-92 cells were not) the effect of BBBD on the endothelium alone is one that at least partially promotes leukocyte extravasation, either by disrupting endothelial tight junctions or through some unknown mechanism. Finally, there may be direct mechanical effects of the oscillating microbubbles on the effector cells that have yet to be elucidated.

In addition to the increased accumulation of HER2-specific NK-92 cells in group 3 tumors, dense accumulations of HER2-specific NK-92 cells around arterioles and venules in group 3 (Fig. 6A and C). Larger vessels may have permitted greater microbubble activity (decreased bubble damping compared with capillary sized vessels, or a bubble population with a mean size closer to the resonant frequency used), or possibly was able

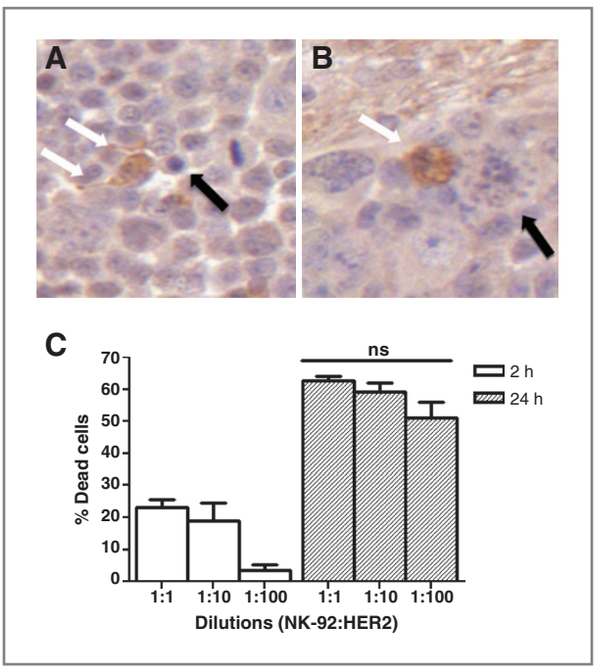

Figure 7. HER2-specific NK-92 cells accumulate at the tumor and have preserved function. A, IHC for granzyme B highlights an NK-92 cell releasing granzyme B into the surrounding extracellular space (white arrows). An adjacent apoptotic tumor cell can be seen (black arrow). B, granzyme B–containing NK-92 cell (white arrow) causing apoptosis in a tumor cell (black arrow). At 24 hours, a 1:100 ratio of effector:tumor cells is statistically no different ($P > 0.05$) in causing tumor cell lysis than higher starting ratios (C). This is the ratio of effector-to-tumor cells that was achieved *in vivo* in group 3.

to support larger inter-endothelial openings. Along capillaries, the effector cells were seen to line the adluminal surface, even in the absence of nearby tumor cells (Fig. 6B and D). We did not see any of these features in group 1 or 2 animals. Of particular note in both ultrasound-treated groups is the absence of erythrocytes among extravasated HER2-specific NK-92 cells (there was a small region of erythrocyte extravasation adjacent the tumor absent effector cells). It is believed this is in keeping with the postulated mechanism for the increased leukocyte extravasation with BBBD. The inter-endothelial openings, only studied post-BBBD, have been shown to be on the order of tens to hundreds of nanometers, and thus much smaller than the diameter of an erythrocyte (18, 44). Erythrocytes are typically dispersed with little adherence to endothelial cells in the face of fluid shear stresses (45), whereas the reverse is true for leukocytes (39–43).

Of significant concern was whether HER2-specific NK-92 cells circulating at the time of the BBBD would maintain their cytolytic function. Figure 6A and C show a large group of extravascular HER2-specific NK-92 cells surrounding an extratumoral venule. In such a vessel (outside the tumor but within the ultrasound focus), the direction of extravasation should be random, but the preferential clustering of cells toward the tumor suggests preserved bioactivity of the cells. Furthermore, perforin and granzyme B IHC provided evidence that these mediators of apoptosis were being released into the intercellular space, and a number of apoptotic cells were identified in close association with HER2-specific NK-92 cells (Fig. 7A and B). In addition to preserved biologic function, we estimated that the effector-to-target cell ratios realized would be sufficient to result in efficient tumor cell lysis (Fig. 7C). Because the SPIO nanoparticle transfection efficiency was less than 100%, the calculated densities likely underestimate the actual number of HER2-specific NK-92 cells reaching the tumors.

We have showed for the first time the feasibility of using targeted immune cells combined with MRI-guided FUS to treat tumors in the brain. This treatment holds significant promise as it is specific not only to the environs of the tumor, but also to the malignant cells themselves, and can be done noninvasively under MRI guidance. Furthermore, theoretically the NK-92 cells could be retargeted to any number of cancer-associated antigens to allow the treatment of a variety of human malignancies. Future studies will aim to show a reduction in tumor volume and an improved survival in brain metastasis-bearing rats, as these are real-world indicators of treatment success. The NK-92 cell line has already been used in early clinical trials (29, 30) and with the expanding clinical testing of FUS, and also the recent demonstration of the safety and repeatability of BBBD in rhesus macaques (23), this treatment has the potential to benefit patients with brain metastasis in the foreseeable future.

Disclosure of Potential Conflicts of Interest

K. Hynynen has a commercial research grant from FUS Instruments and has ownership interest (including patents) in Sunnybrook Research Institute and Brigham and Women's Hospital, and FUS Instruments. No potential conflicts of interest were disclosed by the other authors.

Authors' Contributions

Conception and design: R.D. Alkins, A. Burgess, K. Hynynen
Development of methodology: R.D. Alkins, A. Burgess, M. Ganguly, K. Hynynen
Acquisition of data (provided animals, acquired and managed patients, provided facilities, etc.): R.D. Alkins, A. Burgess, G. Francia, K. Hynynen
Analysis and interpretation of data (e.g., statistical analysis, biostatistics, computational analysis): R.D. Alkins, A. Burgess
Writing, review, and/or revision of the manuscript: R.D. Alkins, A. Burgess, R.S. Kerbel, W.S. Wels, K. Hynynen
Administrative, technical, or material support (i.e., reporting or organizing data, constructing databases): M. Ganguly, W.S. Wels
Study supervision: K. Hynynen

Acknowledgments

The authors thank Meaghan O'Reilly for assistance with the FUS equipment and Rafal Janik for assistance with MR imaging, and Shawna Rideout-Gros and Alexandra Garces for assistance with animal handling.

Grant Support

This research was funded by the National Institutes of Health (R01 EB003268 to K. Hynynen) and the Canada Research Chair Program.

The costs of publication of this article were defrayed in part by the payment of page charges. This article must therefore be hereby marked *advertisement* in accordance with 18 U.S.C. Section 1734 solely to indicate this fact.

Received July 2, 2012; revised November 21, 2012; accepted December 13, 2012; published OnlineFirst January 9, 2013.

References

1. Lee Y-T. Breast carcinoma: pattern of metastasis at autopsy. J Surg Oncol 1983;23:175–80.
2. Lin NU, Bellon JR, Winer EP. CNS metastases in breast cancer. J Clin Oncol 2004;22:3608–17.
3. Abbott NJ, Rönnbäck L, Hansson E. Astrocyte-endothelial interactions at the blood-brain barrier. Nat Rev Neurosci 2006;7:41–53.
4. Lockman PR, Mittapalli RK, Taskar KS, Rudraraju V, Gril B, Bohn KA, et al. Heterogeneous blood–tumor barrier permeability determines drug efficacy in experimental brain metastases of breast cancer. Clin Cancer Res 2010;16:5664–78.
5. Linn SC, Giaccone G, van Diest PJ, Blokhuis WM, van Der Valk P, van Kalken CK, et al. Prognostic relevance of p-glycoprotein expression in breast cancer. Ann Oncol 1995;6:679–85.
6. Slamon DJ, Clark GM, Wong SG, Levin WJ, Ullrich A, McGuire WL. Human breast cancer: correlation of relapse and survival with amplification of the HER2/neu oncogene. Science 1987;235:177–82.
7. Slamon DJ, Leyland-Jones B, Shak S, Fuchs H, Paton V, Bajamonde A, et al. Use of chemotherapy plus a monoclonal antibody against HER2 for metastatic breast cancer that overexpresses HER2. N Engl J Med 2001;344:783–92.
8. Geyer CE, Forster J, Lindquist D, Chan S, Romieu CG, Pienkowski T, et al. Lapatinib plus capecitabine for HER2-positive advanced breast cancer. N Engl J Med 2006;355:2733–43.
9. Smyth MJ, Hayakawa Y, Takeda K, Yagita H. New aspects of natural-killer-cell surveillance and therapy of cancer. Nat Rev Cancer 2002;2:850–61.
10. Uherek C, Tonn T, Uherek B, Becker S, Schnierle B, Klingemann H-G, et al. Retargeting of NK-cell cytolytic activity to ErbB2 expressing tumor cells results in efficient and selective tumor cell destruction. Blood 2002;100:1265–73.
11. Daldrup-Link HE, Meier R, Rudelius M, Piontek G, Piert M, et al. *In vivo* tracking of genetically engineered anti-Her2/neu directed natural killer

cells to Her2/neu positive mammary tumors with magnetic resonance imaging. Eur Radiol 2005;15:4–13.
12. Meier R, Piert M, Piontek G, Rudelius M, Oostendorp RA, Senekowitsch-Schmidtke R, et al. Tracking of [18F]FDG-labeled natural killer cells to HER2/neu-positive tumors. Nucl Med Biol 2008;35:579–88.
13. Pestalozzi BC, Brignoli S. Trastuzumab in CSF. J Clin Oncol 2000; 18:2350–1.
14. Stemmler HJ, Schmitt M, Willems A, Bernhard H, Harbeck N, Heinemann V. Ratio of trastuzumab levels in serum and cerebrospinal fluid is altered in HER2-positive breast cancer patients with brain metastases and impairment of blood-brain barrier. Anticancer Drugs 2007;18: 23–8.
15. Polli JW, Humphreys JE, Harmon KA, Castellino S, O'Mara MJ, Olson KL, et al. The role of efflux and uptake transporters in [N-{3-chloro-4-[(3-fluorobenzyl)oxy]phenyl}-6-[5-({[2-(methylsulfonyl)ethyl]amino} methyl)-2-furyl]-4-quinazolinamine (GW572016, lapatinib) disposition and drug interactions. Drug Metab Dispos 2008;36:695–701.
16. Hynynen K, McDannold N, Vykhodtseva N, Jolesz FA. Noninvasive MR imaging-guided focal opening of the blood–brain barrier in rabbits. Radiology 2001;220:640–6.
17. McDannold N, Vykhodtseva N, Hynynen K. Use of ultrasound pulses combined with Definity® for targeted blood-brain barrier disruption: a feasibility study. Ultrasound Med Biol 2007;33:584–90.
18. Sheikov N, McDannold N, Vykhodtseva N, Jolesz F, Hynynen K. Cellular mechanisms of the blood-brain barrier opening induced by ultrasound in presence of microbubbles. Ultrasound Med Biol 2004;30:979–89.
19. Sheikov N, Mcdannold N, Sharma S, Hynynen K. Effect of focused ultrasound applied with an ultrasound contrast agent on the tight junctional integrity of the brain microvascular endothelium. Ultrasound Med Biol 2008;34:1093–104.
20. Kinoshita M, McDannold N, Jolesz FA, Hynynen K. Noninvasive localized delivery of Herceptin to the mouse brain by MRI-guided focused ultrasound-induced blood-brain barrier disruption. Proc Natl Acad Sci 2006;103:11719–23.
21. Liu HL, Hua MY, Chen PY, Chu PC, Pan CH, Yang HW, et al. Blood-brain barrier disruption with focused ultrasound enhances delivery of chemotherapeutic drugs for glioblastoma treatment. Radiology 2010;255:415–25.
22. Burgess A, Ayala-Grosso CA, Ganguly M, Jordão JF, Aubert I, Hynynen K. Targeted delivery of neural stem cells to the brain using MRI-guided focused ultrasound to disrupt the blood-brain barrier. PLoS One 2011;6:e27877.
23. McDannold N, Arvanitis CD, Vykhodtseva N, Livingstone MS. Temporary disruption of the blood-brain barrier by use of ultrasound and microbubbles: safety and efficacy evaluation in rhesus macaques. Cancer Res 2012;72:3652–63.
24. Francia G, Man S, Lee CJ, Xu P, Mossoba ME, Emmenegger U, et al. Comparative impact of trastuzumab and cyclophosphamide on HER-2-postive human breast cancer xenografts. Clin Cancer Res 2009;15: 6358–66.
25. Kobayashi N, Allen N, Clendenon NR, Ko LW. An improved rat brain-tumor model. J Neurosurg 1980;53:808–15.
26. Chopra R, Curiel L, Staruch R, Morrison L, Hynynen K. An MRI-compatible system for focused ultrasound experiments in small animal models. Med Phys 2009;36:1867–74.
27. O'Reilly MA, Hynynen K. Blood-brain barrier: real-time feedback-controlled focused ultrasound disruption by using an acoustic emissions-based controller. Radiology 2012;263:96–106.
28. O'Reilly MA, Muller A, Hynynen K. Ultrasound insertion loss of rat parietal bone appears to be proportional to animal mass at submegahertz frequencies. Ultrasound Med Biol 2011;37:1930–7.
29. Tonn T, Becker S, Esser R, Schwabe D, Seifried E. Cellular immunotherapy of malignancies using the clonal natural killer cell line NK-92. J Hematother Stem Cell Res 2001;10:535–44.
30. Arai S, Meagher R, Swearingen M, Myint H, Rich E, Martinson J, et al. Infusion of the allogeneic cell line NK-92 in patients with advanced renal cell cancer or melanoma: a phase I trial. Cytotherapy 2008; 10:625–32.
31. Ahmed N, Ratnayake M, Savoldo B, Perlaky L, Dotti G, Wels WS, et al. Regression of experimental medulloblastoma following transfer of HER2-specific T cells. Cancer Res 2007;67:5957–64.
32. Ahmed N, Salsman VS, Kew Y, Shaffer D, Powell S, Zhang YJ, et al. HER2-specific T cells target primary glioblastoma stem cells and induce regression of autologous experimental tumors. Clin Cancer Res 2010;16:474–85.
33. Altland OD, Dalecki D, Suchkova VN, Francis CW. Low-intensity ultrasound increases endothelial cell nitric oxide synthase activity and nitric oxide synthesis. J Thromb Haemost 2004;2:637–43.
34. Hsu S, Huang T. Bioeffect of ultrasound on endothelial cells *in vitro*. Biomol Eng 2004;21:99–104.
35. Deng J, Huang Q, Wang F, Liu Y, Wang Z, Wang Z, et al. The role of caveolin-1 in blood-brain barrier disruption induced by focused ultrasound combined with microbubbles. J Mol Neurosci 2012; 46:677–87.
36. Ward M, Wu J, Chiu JF. Ultrasound-induced cell lysis and sonoporation enhanced by contrast agents. J Acoust Soc Am 1999;5:2951–7.
37. Wu J. Shear stress in cells generated by ultrasound. Prog Biophys Mol Biol 2007 93:363–73.
38. VanBavel E. Effects of shear stress on endothelial cells: possible relevance for ultrasound applications. Prog Biophys Mol Biol 2007; 93:374–83.
39. Dewitz TS, Hung TC, Martin RR, McIntire LV. Mechanical trauma in leukocytes. J Lab Clin Med 1977;90:728–36.
40. Okuyama M., Kambayashi J, Sakon M, Monden M. LFA-1/ICAM-3 mediates neutrophil homotypic aggregation under fluid shear stress. J Cell Biochem 1996;60:550–9.
41. Moazzam F, DeLano FA, Zweifach BW, Schmid-Schönbein GW. The leukocyte response to fluid stress. Proc Natl Acad Sci 1997;94: 5338–43.
42. Kitayama J, Hidemura A, Saito H, Nagawa H. Shear stress affects migration behavior of polymorphonuclear cells arrested on endothelium. Cell Immunol 2000;203:39–46.
43. Cinamon G, Shinder V, Alon R. Shear forces promote lymphocyte migration across vascular endothelium bearing apical chemokines. Nat Immunol 2001;2:515–22.
44. Marty B, Larrat B, Van Landeghem M, Robic C, Robert P, Port M, et al. Dynamic study of blood-brain barrier closure after its disruption using ultrasound: a quantitative analysis. J Cereb Blood Flow Metab 2012;32:1948–58.
45. Yedgar S, Koshkaryev A, Barshtein G. The red blood cell in vascular occlusion. Pathophysiol Haemost Thromb 2002;32:263–8.